SSC17-VI-02

CHIEM: A new compact camera for hyperspectral imaging

Joris Blommaert, Bavo Delauré, Stefan Livens, Dirk Nuyts
VITO – Remote Sensing Department
Boeretang 200, B-2400 Mol, Belgium; +32 14 33 55 11
joris.blommaert@vito.be

Klaas Tack, Andy Lambrechts
IMEC
Kapeldreef 7, B-3001 Leuven, Belgium; +32 16 28 14 36
klaas.tack@imec.be

Vincent Morau
AMOS
Liège Science Park, Rue des Chasseurs Ardennais, B-4031 Angleur, Belgium, +32 4 361 40 40
vincent.moreau@amos.be

Eric Callut, Gérard Habay, Koen Vanhoof, Michel Caubo
Deltatec
Rue Gilles Magnée 92/6, B-4430 Ans, Belgium, +32 4 2397880
e.callut@deltatec.be

Jan Vandenbussche
CMOSIS bvba, AMS
Coveliersstraat 15, B-2600 Antwerp, +32 3 260 17 30
jan.vandenbussche@cmosis.com

Atul Deep, Kyriaki Minoglou
European Space Agency -ESTEC,
Keplerlaan 1, PO Box 299, +31 71 565 6565
atul.deep@esa.int

ABSTRACT

We have developed an engineering model of a novel compact hyperspectral imager. The CHIEM instrument is designed to be compatible with a 12U CubeSat satellite, offering a swath of 100km and a GSD of 25m from 600km altitude. The hyperspectral sensor has thin film interference filters directly deposited on a 12Mpixel CMOS 2D detector array. The spectral range covers 470 to 900 nm, with narrow spectral resolution (FWHM) between 5 and 10nm. Besides the hyperspectral zone which covers 2/3 of the detector array, it also contains 2 panchromatic zones without filters. While the baseline design uses a conventional front-side illuminated CMOS sensor, the development also includes filter depositions on a back-side illumination (BSI) version with a higher sensitivity. For the optical design of the front telescope, CHIEM uses a very compact three mirror anastigmat, which allows a wide field of view in both across track and along track direction (> 9.5^o x 7.2^o). The readout electronics (ROE) provides all required sensor interfaces (power, control, data) enabling its full performance operation, and also a set of backend interfaces for system power, remote control, and backend remote data (to EGSE) and local storage interfaces.

INTRODUCTION

In the CHIEM project we have developed an instrument for remote sensing which addresses two important trends in the space business in recent decades: the demand for detailed spectral information and the need to build smaller and cheaper satellite platforms. CHIEM stands for **C**ompact **H**yperspectral **I**nstrument

Engineering **M**odel. Spectral observations allow detailed studies in different areas like water quality, land cover, land use and climate change. Current operational hyperspectral missions are Hyperion and CHRIS [1]. New developments giving higher sensitivity and better spectral coverage are for example EnMap, HyspIRI and PRISMA [2,3,4]. These missions are also quite large in size, have a relatively low revisit rate, are expensive and complex. They are built and operated by space agencies.

An earlier, successful example where a much smaller satellite replaced a larger one is PROBA-V. This multispectral imaging mini-satellite provides global land cover and vegetation monitoring every two days for the entire planet [5,6]. Nowadays, further instrument miniaturization allows the industry to develop extremely small remote sensing satellites on CubeSat platforms. One example of such a commercial initiative is the one by the American company Planet Labs, Inc. They aim to offer imaging of the Earth using a cluster of CubeSats at 3-5 m resolution and daily coverage. The latter examples however only provide multispectral imaging and lack spectral detail.

With the CHIEM project we develop an instrument allowing to combine both: imaging with high spectral resolution with an instrument that is 12 U CubeSat compatible. With this instrument the hyperspectral imaging is obtained with a so-called Linear Variable Filter (LVF) directly deposited on a 2D sensor array. The cross-track dimension of the array provides the spatial information, whereas the along-track dimension registers the spectral information. As is schematically shown in Figure 1, a spectrum over the full provided wavelength range is obtained by scanning the array along track at the appropriate frame rate.

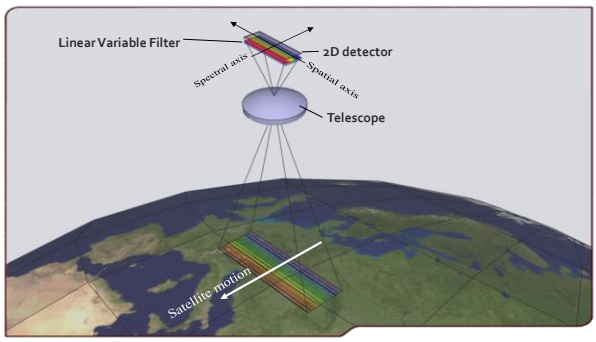

Figure 1 : Schematic overview of the scanning technique with a LVF-based satellite instrument

The baseline instrument design is for a satellite mission operating at 600 Km, but also alternative operational scenarios of the imager, such as airborne application are taken into account in the development. An overview of the relevant parameters for two scenarios is given in Table 1. The wavelength coverage of the spectrometer is at least 470 – 900 nm

Table 1: Overview of parameters for the baseline satellite design and for an airborne application.

Baseline satellite design			Airborne
Altitude	600	[km]	5
Ground speed	6900	[m/s]	66
Swath	100	[km]	2.4
Focal length	135	[mm]	45
GSD	24.4	[m]	0.6
Line time	3.5	[ms]	9

The concept of a very small LVF-based hyperspectral satellite was first proposed in the *PhytoMapper* project [7] and then further refined, including a separate panchromatic detector to combine the acquisition of high spatial resolved information with hyperspectral information [8]. Similar concepts, targeting a CubeSat platform, are described in [9,10]. Around the same time, advancements in microelectronics technology showed the possibility to create hyperspectral imagers based on interference filters using a new technique in which filter material is deposited directly onto the detector. This process has a number of advantages compared to the traditional LVF filters. It allows a lot of design flexibility up to defining individual filters at single pixel level. At the same time it is possible to define different zones at an individual detector with different functionality, for instance a combination of spectral zones with panchromatic zones. Moreover, it offers improved performance compared to classical LVF filters by better alignment and reduced straylight.

The practical feasibility of this process was demonstrated on a 2Mpixel CMV2000 sensor from CMOSIS using a single filter stack, resulting in a spectral range of 600nm-900nm [11]. This sensor-filter combination has spurred considerable interest, most notably for instruments aboard small remotely piloted aircraft system platforms. An example of such a camera is the COSI-Cam (COmpact Hyperspectral Imaging System) [12,13]. The COSI spectral imager has been operated by VITO for agricultural purposes to derive different parameters like chlorophyll content, biomass and hydric status indicators. The COSI system provides

accurate action and information maps related to the crop status [14]. An illustration of the COSI images and hypercube data is shown in Figure 2.

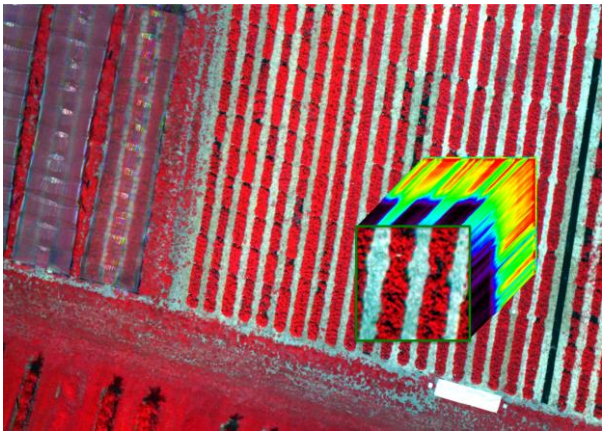

Figure 2 : An illustrative example with a false colour image and a hyperspectral data cube, obtained with the COSI-cam above an agricultural field (strawberry) [12,13,14]. Each pixel in the image contains a continuous spectrum.

From the above experience, it was also evident that extending the visual spectral range coverage would greatly increase the usefulness. To realize this, the ESA project FIDELHEO (FIlter DEposition for Lightweight Hyperspectral Earth Observers) was initiated and performed by IMEC and VITO. From the start, the aim of the FIDELHEO project was to design and produce a hyperspectral imager optimized for Earth observation purposes [15]. This starting point has guided the design choices made during development. To cover a wider spectral range of 470-900nm, it was necessary to use a more complex filter deposition in which two filter stacks are used, each of a different material. The project was successful and is nowadays used in commercial cameras like the ButterflEYE LS (Cubert GmbH) and Imec's Snapscan.

While FIDELHEO-like hyperspectral filters are very well suited for Earth observation from aerial platforms, employing them efficiently for imaging from space would greatly benefit from a detector which offers a larger number of pixels in the across-track direction, enabling wider swath imaging for a fixed resolution. This was the first reason to initiate a new ESA project, called CHIEM, targeted at making interference hyperspectral imagers more suitable for space applications. The project is not limited to just hyperspectral filter development, but also the design of the other necessary subsystems to match them.

In the CHIEM development of the compact hyperspectral instrument from breadboard to engineering model by implementing a number of important improvements for the different subsystems. The ESA project is funded by BELSPO and is carried out by a consortium of Belgian companies with the following responsibilities:

- System engineering activities to refine the conceptual design of the Compact Hyperspectral Instrument and to complete the end-to-end performance analysis (VITO).
- Opto-mechanical design, including telescope, Focal Plane Assembly, baffling, and thermo-mechanical I/F (AMOS).
- Modification of an existing large format CMOS sensor design to allow the deposition of Fabry-Pérot filters at wafer level (CMOSIS).
- Improvement of the Linear Variable Filter (LVF) to match the detector format and requirements of out-of-band rejection (IMEC).
- Deposition of LVF filters on BSI sensors (IMEC).
- Development of the detector read-out electronics and of the relevant electrical I/F (Deltatec).
- Development of the EGSE to interface the read-out electronics to standard computer (Deltatec).
- Testing and verification of the fully assembled focal plane assembly

At present (June 2017), the CHIEM project is in its final phases, where the opto-mechanical design is finalized, as well as the manufacturing of the ROE and EGSE of the system. The characterization campaign of the produced BSI and FSI sensors has started. Analysis of the test campaign is expected to be finalized in the Summer of 2017.

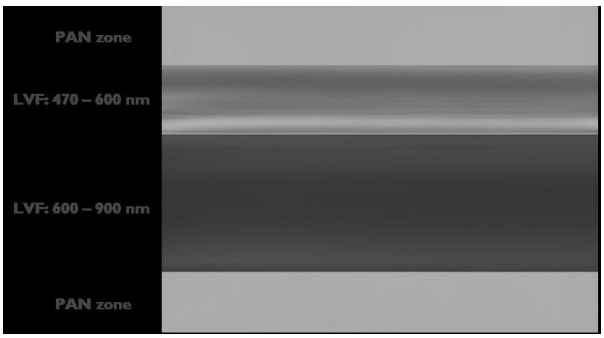

Figure 3: First CHIEM hyperspectral FSI sensor image

In the following sections the different aspects of the instrument are further described in more detail.

CMOS SENSOR

With the targeted application in mind, the system specifications have been translated to sensor specifications and compared to proven CMOS imager products. Finally the CMV12k was selected. The CMV standard product series serves a broad range of industrial vision, movie, traffic monitoring and motion controlled applications. Here for the sensor is equipped with an 8T global shutter pixel structure as shown in Figure 4. This pixel combines pipelined global shutter operation with CDS [16].

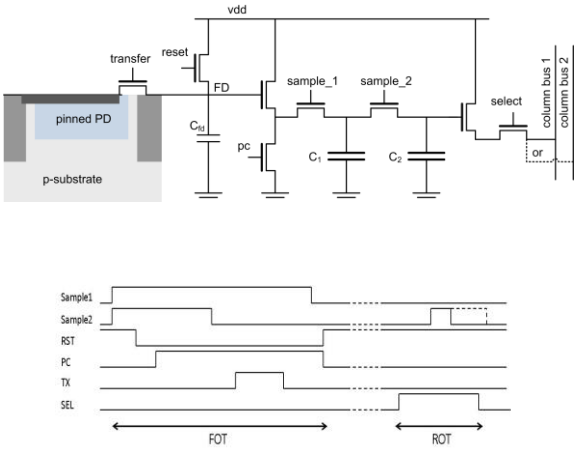

Figure 4: Pixel architecture and operation.

The image sensor architecture is shown in Figure 5. The pixel array measures 4096 by 3072 pixels at 5.5 µm pitch. With a dual readout on the top and bottom of the sensor, a global throughput rate of 36 Gbps for this 12Mpixel sensors is achieved in a 10bit resolution at approximately 300 frames/s.

The CMV12k sensor was used both for FSI and BSI filter post processing; adding hyperspectral filters designed for the targeted applications. The BSI route offers the advantage of higher sensitivity and an eliminated ripple on the Quantum efficiency (see next section).

Some samples from the FSI route were characterized before deposition of the filters; so no color filters, nor micro lenses were deposited on the measured samples. The most important measured characteristics of the achieved performance of this sensor (FSI, without hyperspectral filters) is listed in Table 2.

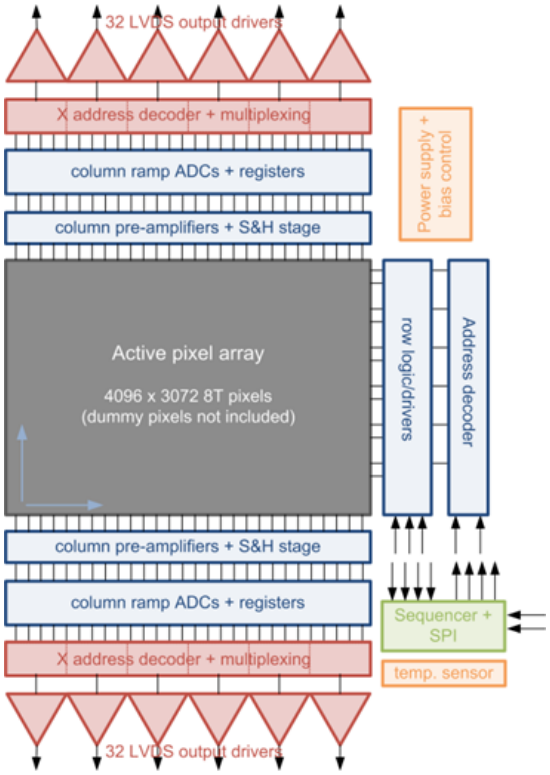

Figure 5: Image sensor architecture.

Table 2: CMV12k Sensor Performance

Specification	Value	Measured	Unit
Pixel size	5.5	-	um
Resolution	4096x3072	-	px
Frame rate	300 @ 10bit 132 @ 8bit	-	fps
Read noise at 25°C, default gain	25	16	e^-
Dark current at 25°C die temperature	<100	<100	e^-/s
Quantum Efficiency	50	20 (1)	%
Full Well	10	9.4	ke^-
Dynamic range	60	55.5	dB
Power consumption	3	2.2	W

Note (1): Test silicon in this work was starting material for further hyperspectral filter processing and not equipped with microlenses.

LINEAR VARIABLE FILTER

introduction

In the traditional approach, narrow band linear variable filters are typically deposited on a glass substrate and then integrated separately with the sensor (e.g. as cover glass). This approach has several disadvantages related to the integration of the filter with the sensor. First, reflections between the Linear Variable Filter and the focal plane array make it more sensitive to stray light and second, the alignment of the filters with the pixels is not obvious. These disadvantages can be eliminated by depositing the filter directly on the focal plane array, using typical semiconductor process tools guaranteeing accurate alignment and removing additional reflection. An example of a wafer with imager and optical filters is shown in Figure 6.

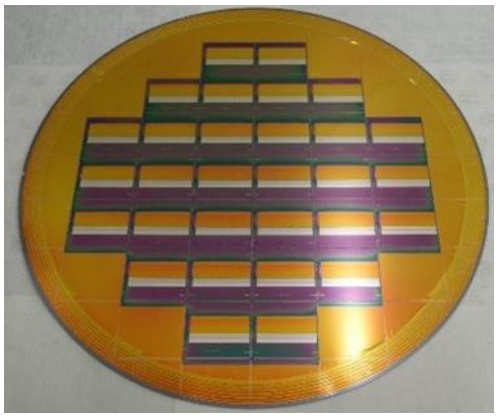

Figure 6: CMV12000 wafer: image sensor with integrated optical filters

An additional advantage of this approach is the freedom for the layout of the filters on the focal plane array. Indeed, using our technique, every pixel has its own narrow band filter and selecting the layout is only a matter of designing the correct masks.

Figure 7: CMV12000 imager with integrated hyperspectral filter bank and panchromatic zone

As shown in figure 7, this enabled us to combine different stripes on the imager with different functionality. The gold colored part of the chip on the top and the bottom is a panchromatic zone, combined with a grey colored hyperspectral zone in the center of the chip.

Filter design

A first important aspect of the filter design is to select a filter architecture that matches the typical operations of semiconductor process technology, i.e. deposit a film, pattern the film using lithography and remove the unwanted part using an etch process. The hyperspectral sensor presented in this paper therefore implements an approximation of a Linear Variable Filter (LVF) using a set of Fabry-Pérot filters. Figure 8 illustrates the typical Fabry-Pérot Filter made of a transparent layer (called cavity) with two mirrors at each side of that layer. The mirrors are Bragg reflectors consisting of a multiple layer stack of alternating high and low refractive index materials. The reflectivity of these mirrors defines the spectral range, the Full Width Half Max (FWHM) and the quality of the filter. The cavity thickness *t* defines the central wavelength of the optical filter.

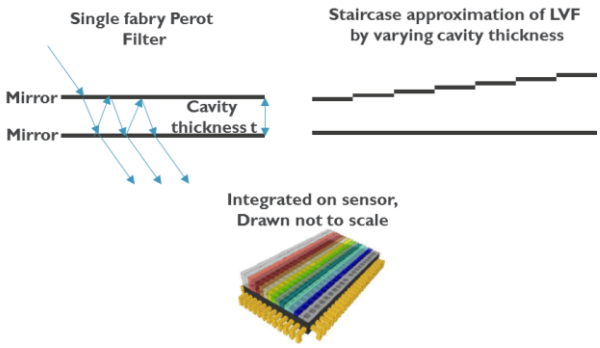

Figure 8: the presented hyperspectral sensor relies on the use of Fabry-Pérot filters post-processed on top of the CMOS imager.

As illustrated in Figure 8, the spectral filters are arranged with cavities in a wedge or staircase-like structure in which each step of the wedge acts as an independent optical filter. To reduce the number of process steps, the Bragg mirrors are shared between all filters and only the cavity thickness is varied. The spectral range of the Fabry-Pérot filter is therefore limited by the bandwidth of the Bragg mirror. An important parameter in the design of the Linear Variable Filter is the selection of the material combination for the Bragg mirrors, which shall be materials compatible with CMOS (in terms of thermal budget [17,18] and contamination level).

The combination of the selected filter architecture and the available CMOS-compatible materials enable a spectral range covering 470 nm to 900 nm. The full range can however not be covered with one Bragg stack. For this reason, the sensor is integrating two wedges, completely independent from each other, each using a different built-up for their Bragg reflectors. The first wedge covers the range from 470-620 nm, while the second wedge covers from 600 up to 900 nm. The ~20 nm overlap allows to cope with deposition tolerances and enables a smooth spectral acquisition across both ranges.

The selection of the specific bands, i.e. thickness selection of the cavities, is done by adapting the sampling rate to the FWHM of the optical filters, i.e. the sampling distance between two filters is slightly lower than the FWHM of the filters. At the edges of the spectral range, the FWHM of the Fabry-Perot filters is increasing enabling a decrease of the sampling rate. This results in 104 bands for the wedge covering 600 nm to 900 nm and 50 bands for the wedge between 470 nm and 600 nm. The simulation results are shown in Figure 9, visualizing a spectrogram, i.e. the spectral response of all the filters shown as color intensity variations. The lines in the spectrogram represent the bands, while the columns in the spectrogram represent the wavelengths. Dark blue means low transmission, while brighter colors represent higher transmission.

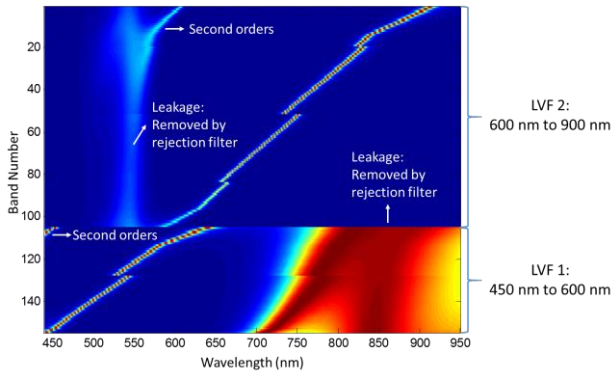

Figure 9: Selection of patterning procedure – location of filters spread over spectral range. Filter responses are shown as color intensity with the lines representing the spectral bands and the columns representing the wavelength. Spectral responses are the responses of the Fabry-Pérot filters only before applying the rejection filters

A schematic layout of the sensor with the two wedges can be observed in Figure 10. As already mentioned, the image sensor used is the CMOSIS CMV12000. This sensor has 4096 x 3072 pixels. To maximize the SWAT, we have selected the dimension with 4096 pixels as the width of the sensor. Because of the high number of rows in the CMV12000 sensor, multiple lines can be grouped per band. It is important for the synchronization of the frame rate of the camera to the speed of the scanned object, that the number of lines per band is the same in both wedges. We have chosen to assign 12 lines to every band, resulting in 600 lines for LVF1 and 1248 lines for LV2. The remaining lines are spent on two PAN zones at the top and the bottom and 1 dead zone of 72 lines.

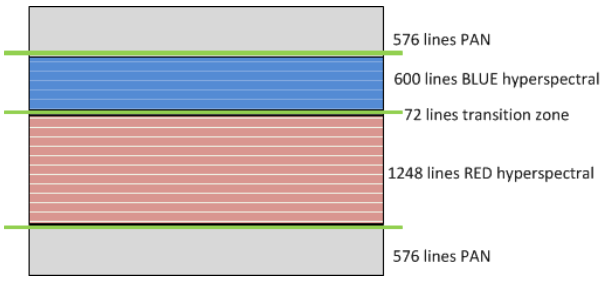

Figure 10 Layout of the two wedge filters on the CMV12000 sensor, with 50 'blue' and 104 'red' spectral bands.

As can be seen in Figure 9, both LVF's have significant leakage of light outside their own spectral range, but still inside the range of the combined LVF. The following blocking filters integrated with the LVF are therefore needed to remove this leakage:

1. A low pass filter LVF 1 (450 nm to 650 nm), removing all leakage above 680 nm.
2. A high pass filter on LVF 2 (600 nm to 900 nm), removing all leakage below 580 nm.

Figure 11 shows a schematic cross-section of this sensor, with the two independent filter banks or wedges (wedge 1 covering 470-620 nm and wedge 2 for the 600-900 nm range), which are co-fabricated on the same imager wafer.

Two options were implemented for the integration of the rejection filter, enabling a comparison of the performance of both approaches:

1) Hybrid integration, the low-pass and high-pass filters are deposited on a glass substrate and epoxied on top of the monolithic LVF
2) Monolithic integration, the low-pass and high-pass filters are deposited directly onto the LVF

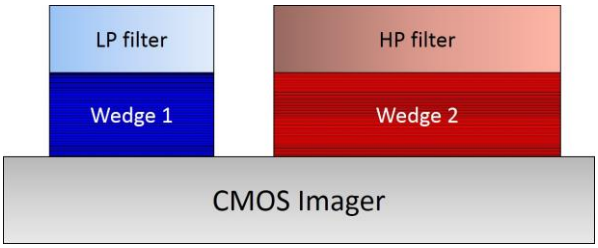

Figure 11: Schematic cross-section of the sensor, with the two wedges (wedge 1 and wedge 2 covering 470-620 and 600-900 nm respectively) post-processed on top of the incoming CMOSIS CMV12000 imager. The rejection filters, an LP to be integrated on top of wedge 1 and an HP to be integrated on top of wedge 2, are also shown. Dimensions not to scale.

In the case of hybrid integration, the rejection filter was deposited on a glass substrate which is thin enough to fit in the CMV12000 standard package. The high-pass and low-pass filter were deposited on separate glass substrates, diced and epoxied together to form one piece. Figure 12 shows a cross section of the chip with the hybrid integrated filters (illustrated on one of the two wedges for clarity). The rejection filter is epoxied on top of the LVF filter with a typical distance between the rejection filter and the LVF of 100 µm. Calculated from the filter to the focal plane array, this distance results in a maximum allowable half cone angle of 60 degrees. The 72 lines transition zone in between the red and blue zones are used as space to cope with tolerances on alignment and dimensions of the additional filters.

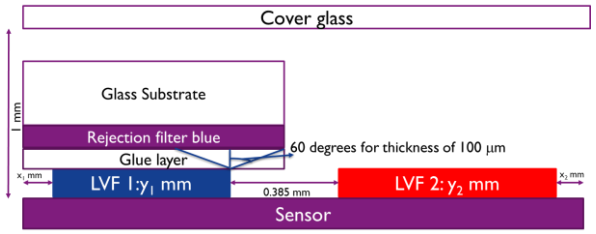

Figure 12: Option 1 – glue rejection filter on the LVF (shown for LVF 1 only)

In the case of the monolithic integration, the low-pass and high-pass filters integrated on LVF 1 and LVF 2 are directly deposited onto the LVF using the same tools and materials.

The most important design option for this filter is the selection of the cut-off wavelength. The reasoning for this cut-off wavelength is determined by the free spectral range of both LVF's in order to have a clean spectral response in the full spectral range. The final simulation results are shown in the spectrogram of Figure 13.

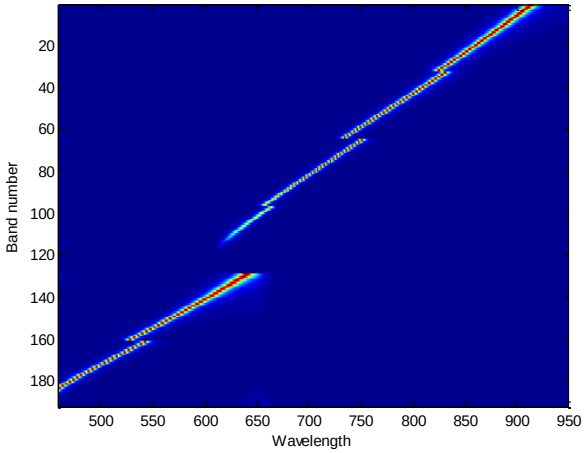

Figure 13: Simulation of final spectrogram after applying the rejection filters

Filters on backside illuminated sensors

Backside Illuminated (BSI) Sensors have the advantage of higher Optical Efficiency compared to FSI imagers. Indeed, because of the metal lines on top of the photosensitive area, the fill factor of an FSI imager is limited, reducing the sensitive area and thus Optical Efficiency (often expressed reduced QE after applying fill factor). BSI imagers are not illuminated through the metal lines on top of the sensor, but from the back where nothing covers the photosensitive area. The fill factor is therefore 100% and the optical efficiency of a BSI imager will always be higher compared to FSI imagers. The higher sensitivity that can be reached is the main reason why we are currently developing a process for the deposition of the optical filters on BSI imagers. This is however not the only reason.

FSI imagers have an isolating and transparent material between the metal lines covering the photosensitive area. This is introducing a thick layer in the optical path that causes additional internal reflections between the photosensitive area and the top layer of the image sensor. These reflections interfere with each other causing a ripple in the QE plot of the imagers as function of wavelength (as illustrated in Figure 14). BSI imagers do not have this transparent material on top of the photosensitive area and will therefore not suffer from these additional reflections, eliminating the ripple on the QE plot. The difference in spectral response between filters on FSI and filters on BSI imagers is

shown in Figure 15. The blue curve has a maximum transmission around 480 nm and shows some additional ripple on its spectral response. The green curve is the spectral response of the filter on top of a BSI imager. In this case, the efficiency is much higher and the spectral response does not show any ripple before 700 nm. Silicon has an absorption index that decreases with wavelength. Depending on the thickness of the silicon in the photosensitive area, some part of the light is no longer fully absorbed by the silicon in the BSI imager. This light is entering the silicon of the photosensitive area, partially reflected on the metal lines/transparent material at the other side and interfering with light at the first interface. This is why some ripple will still occur in the NIR wavelengths.

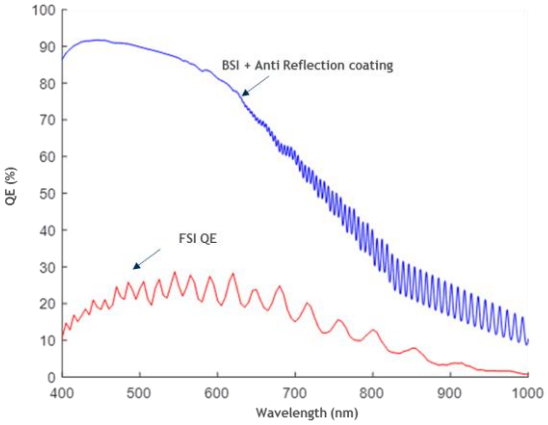

Figure 14: Quantum Efficiencies for the FSI (in red) and BSI (in blue) sensors, with fringe visibility.

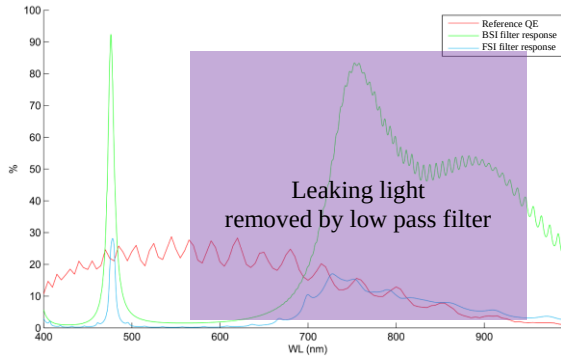

Figure 15: FSI (in blue) vs BSI (in green) filter responses and reference FSI QE (in red).

READOUT ELECTRONICS

ROE general description

The CMV12000 CMOS image sensor capable of 300fps of frame rate at 10-bit of depth. To achieve this throughput, pixels are output on 64 high speed LVDS links running at 600 Mbps, for a total of useful data rate of 37.75 Gbit/s. For real-world use, this high amount of data needs to be compressed before being transmitted. To achieve an efficient compression, the raw image of the sensor is first corrected for per pixel gain and offset variations and not responsive pixels are replaced. All of these computations are done on the camera itself. After that, the image compression can be done.

The required processing on the data is the following:

- Fixed Pattern Noise (FPN) correction (offset)
- Photo Response Non Uniformity (PRNU) correction (gain)
- Bad pixel replacement
- Binning
- Raw image accumulation for calibration map generation
- Cropping of the image (image width reduction)

All these corrections have to be done at full speed, requiring high-speed parallel data processing. Each processing step can be enabled or disabled on request. On the back-end, the processed data is downloaded to the EGSE using **8 high-speed 3G-SDI** (3 Gigabit Serial Digital Interface) uncompressed video links. This interface allows to have access to the full-quality images for analysis but could be replaced by lower-speed RF links using prior compression for real-world use.

The sensor configuration is such that the throughput to the storage system will not be higher than ~18 Gbits/s. Nevertheless for a short period of time, the sensor could be used at its highest frame rate. In this case the images are stored in the internal ROE DDR3 memory (running at 1600 MHz) and are downloaded afterwards to the storage system.

To be able to cope with this high data throughput and high speed parallel data processing, the ROE is based on the Zynq-7000 SoC from Xilinx. This device encapsulates a FPGA (Programmable Logic) and a dual-core ARM Cortex-A9 hardware processor

(Processing System), with hardwired high-speed connections between them. The programmable logic is used to interface the sensor, to process the data and to download it to the EGSE. The processing system manages all high-level (control) aspects of the camera and connects to the EGSE for the TM/TC link.

ROE modularity

The ROE consists of an assembly of 3 boards:

- The first (top) board, also called *Sensor Interface Board (SI Board)*, contains the sensor, the passive components and the voltage converters.
- The second (middle) board, also called *Frame Grabber and Processing Board (FGP Board)*, is the heart of the ROE. It contains the SoC, all its peripherals (DDR memories, Flash memories) and voltages converters.
- The third (bottom) board, also called *External Interface and Power Board (EIP Board)*, will contain all the interface connectors: SDI drivers and connectors, Ethernet connector and PHY, primary power connector and Micro-SD Card slot.

The ROE is modular: the 3G-SDI interface could be replaced by SATA interface or by a compression board without modification of the *frame grabber processing board* and/or *the sensor interface board*.

Use of the Zynq internal functions

As explained the Zynq contains programmable logic and a processing system. The programmable logic implements the interfacing to the sensor, to the 8x 3G-SDI links and to the FPGA dedicated DDR3 memory (1 GByte @ 1600 MT/s). The FPGA is also doing all of the image processing mentioned before.

The processor side of the Zynq takes care of the lower speed interfacing to the outside world (UART, Ethernet and SD card), the booting and configuration of the FPGA part and the management of the correction maps. For all of this, it has its own working memory of 1 GB @ 1066 MT/s.

ROE Features

As mentioned before, the ROE is doing real time image processing on the image stream. To cope with the pixel rate of +/- 3.5 Gpixels/s, the implementation of the image correction (FPN and PRNU), pixel accumulation and the bad pixel replacement is done for 64 pixels in parallel. This part of the processing runs at a frequency of 200 MHz in order to have a few clock cycles per pixel.

To make optimal use of the FPGA resources, the pixel correction and averaging is implemented in a single DSP block per pixel. The pixel accumulation and pixel correction are calculated in 2 clock cycles: during the first cycle the pixel correction is calculated; in the next cycle the pixel accumulation is done. To achieve that, the DSP block implements the following function:

*P = (Pixel – FPN) * PRNU + Accumulated Pixel*

This formula maps perfectly on the resources of the DSP block available in the programmable logic of the Zynq. The block diagram of a Zynq DSP block is shown below.

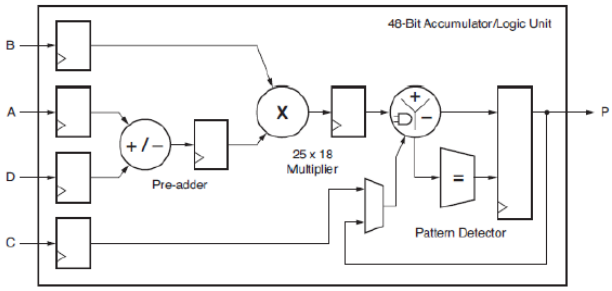

Figure 16: The block diagram of a Zynq DSP block.

With

D as the Pixel Raw value (12 bits)

A as the Pixel Offset (FPN) value (12 bits) or 0 in case of image accumulation

B as the PRNU value (12 bits) or 1 in case of image accumulation

C as the already accumulated pixel value (24 bit) or 0 in case of image correction

P as the Pixel with FPN/PRNU Correction value (12 bits) or the Accumulated Pixel (24 bit)

In order to improve further compression possibilities bad pixel replacement replaces a bad pixel by one of its 8 neighbouring pixels. To implement this a lot of DSP blocks are used to create large multiplexers, running at 200 MHz. The replacement logic of one pixel uses 4 DSP blocks so in total the bad pixel replacement alone uses 256 DSP blocks.

The ROE uses the ROI (Region of Interest) feature of the sensor to limit the height of the image if needed. Up

to 10 different ROIs can be defined on the sensor to create an image which only contains useful information.

Where the ROI feature can only select complete sensor lines, the cropping step allows to tailor the size of the image further. The cropping is the last step in the image processing and reduces the image width of the complete image to a user defined size.

Because the analog binning function which is provided by the sensor is not flexible enough, the ROE provides a binning feature to the following modes: 2x2, 3x3, 4x4 and 6x6.

DDR3 memory bandwidth

Doing all of the image processing in parallel, this results in large data bandwidth requirement for the DDR3 memory which stores the image correction data, the accumulated image data and the video buffers for the 8x3G-SDI links.

To sustain all of the processing in the most demanding use case (doing raw image accumulation while streaming corrected images over SDI), the DDR3 memory needs to sustain a data rate of +/- 90 Gbps to get/deliver the data from/to 5 different sources/sinks at the same time. The implementation uses a fully pipelined AXI interconnect of 512 bits and local buffering, resulting in a DDR3 efficiency of more than 86%.

To a space qualified design

The current requirements (data bandwidth, image correction …) could not be satisfied with available space qualified technologies. Nevertheless new products with better performance are coming on the market. This will be assessed during future development.

One interesting approach is the Hybrid System Architecture using :

- **COTS components** for the data processing requiring high speed processing resources (based on Mil grade latest generation devices like Xilinx 7 or Zynq family + DDR2/3 memory).
- Simpler **RadHard devices** to monitor and manage the COTS devices
- **RadHard** Flash memory, power conditioning …
- Fault Tolerant mechanisms: ECC, scrubbing, internal & external watchdogs, …

EGSE design

CHIEM's ROE is connected to the computer through 8x SDI links for the image grabbing and through a 10/100 Ethernet interface for the TM/TC.

TM/TC interface

The 10/100 Ethernet Interface of the computer will be used for the TM/TC.

Data Interface

The 2 PCIe Delta-3G-elp-d-40 from DELTACAST are used for the video grabbing.

http://www.deltacast.tv/products/developer-products/sdi-cards/delta-3g-elp-d-40

Data Storage

In order to not reduce the system performances in terms of data rate, the EGSE stores the grabbed images at a data rate up to 30Gbps (3.75 GBps).

Currently, best performance is met with 4 NVME SSD disks with a software strip configuration.

Results

The ROE operates typically in 3 different use cases:

1) Recording use case: recording raw frames from the sensor in the DDR3 memory at the highest possible frame rate and the highest possible resolution (12Mpixels)
2) Streaming use case: streaming images from the sensor to the 8x 3G-SDI interface while doing image correction, binning and cropping with a resolution of 4096 x 1920 pixels.
3) Accumulation use case: is the same as the streaming use case but combined with image accumulation of not corrected images. All of this at a lower frame rate than in the streaming use case, with 12 bit pixels and a resolution of 4096x1920 pixels

Final testing of the ROE showed the following results:

Table 3: Achieved frame rates (fps) for the three different use cases given for the different bit depths.

Pixel bit depth	Recording	Streaming	Accumulation
8	328	150	NA
10	294	125	NA
12	130	124	99

OPTICAL DESIGN

A full reflective Three Mirror Anastigmatic design is selected as baseline for the front telescope. This off-axis design, both in aperture and field, is compact, completely unobscured, relatively fast (F/4.5) and diffraction limited over a large field of view, i.e. 7.2° along track and 9.5° across track.

The proposed TMA optical layout is shown in Figure 17. The TMA fits within a 200x200x100 millimeters volume. M1 and M3 are strongly aspherical concave mirrors, while M2 is a spherical convex mirror.

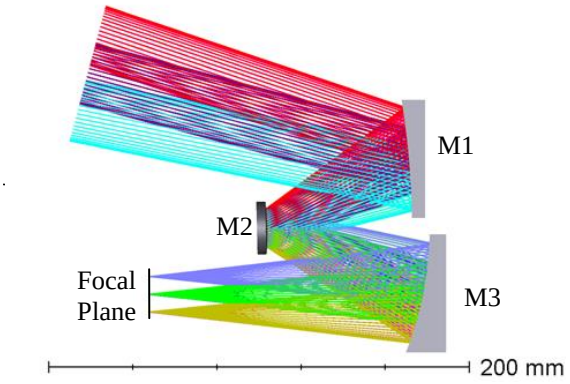

Figure 17 : Optical Layout of the CHIEM front telescope

The focal length of the Telescope is 135 mm, with an entrance pupil diameter of 31 mm. The design is telecentric with an exit pupil located further than 1.5 meter behind the focal plane.

A similar compact TMA has been manufactured by AMOS in optical quality aluminum for the multispectral Proba-V instrument [6], using ultra-accurate single point diamond turning technology. The instrument is fully a-thermal as all elements are made in the same material.

Image Quality

The Image quality has been optimized for different FoV positions at Nyquist frequency 91 lp/mm corresponding to 5.5 µm pixels. The spot diagram over the detector is presented in Figure 18. The optimization also considers the evolution of wavelength from line to line, according to the variable transmission band of the LVF.

The MTF (Modulation Transfer Function) at Nyquist frequency 91 lp/mm range from 0.6 @ 470nm to 0.4 @ 900nm, considering manufacturing and alignment tolerances. These tolerances are quite severe (<10µm on mirror positions and 10 arcsec in tilts, < 20 nm rms surface error) due to the small pixel size.

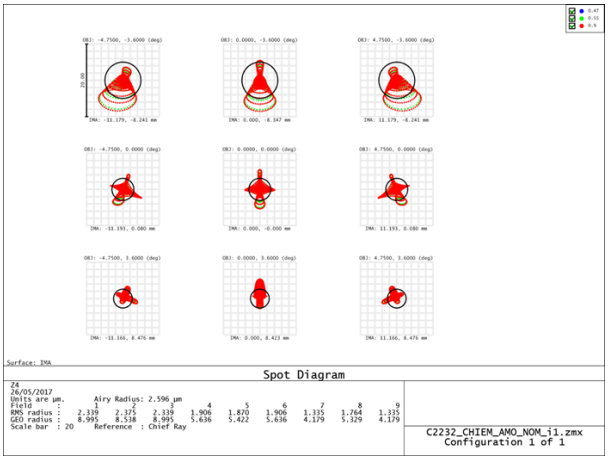

Figure 18 : Spot diagram over the detector. Airy disk is also represented for the LVF wavelength at the corresponding FoV.

Image Distortion

The distortion can be decomposed in *swath curvature* and *keystone* components. Swath curvature will result in non-straight pixels lines on the ground, that can be corrected through image post-processing. Swath curvature values for each channel are given in Figure 19. The keystone will impact inter channel pixel co-registration. The telescope design has been optimized to reduce keystone. However, as the along track field of view is wide it cannot be totally eliminated. The keystone values are given in Figure 20.

Such values of keystone and swath curvature are too large for direct recombination of the complete hyperspectral image stack. Resampling of the individual bands will be necessary for good spatial registration, but the distortions remain sufficiently low for not impacting the addition of up to 12 successive bands, as foreseen for SNR improvement by digital TDI.

Transmittance and Polarization sensitivity

Proposed coating is a Space Qualified Protected Silver Coating from Cilas (France). This coating is well adapted to metallic mirrors and was applied for the Proba V instrument. The analyses consider the measured variations of coatings reflectance with wavelength, incidence angle and light polarization.

From the optical model the total transmittance for both P and S polarization can be computed, taking into account the reflection angle of each single ray on the three mirrors. The results of this calculation are presented in Figure 21.

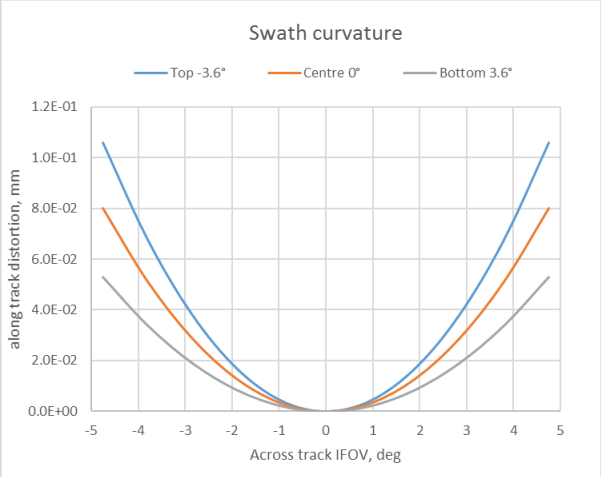

Figure 19 : Swath curvature distortion (in mm on focal plane) for different along track FoV

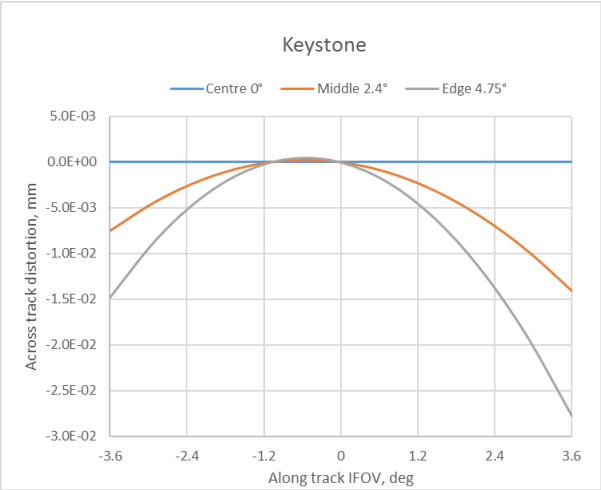

Figure 20 : Keystone distortion (in mm on focal plane) for different across track FoV.

The total transmittance is going from 80% in the blue to 85% in the NIR. The change of transmittance over the across track FoV is negligible (about 0.1%).

From the P and S data, we can evaluate the polarization sensitivity of the telescope, using the formula

$$P_{sens} = \left| \frac{S - P}{S + P} \right| \qquad (1)$$

The computed maximum polarization sensitivity is about 1.3% in the blue. The dependency of this sensitivity with the FoV is very low (< 0.2% change over the across track FoV).

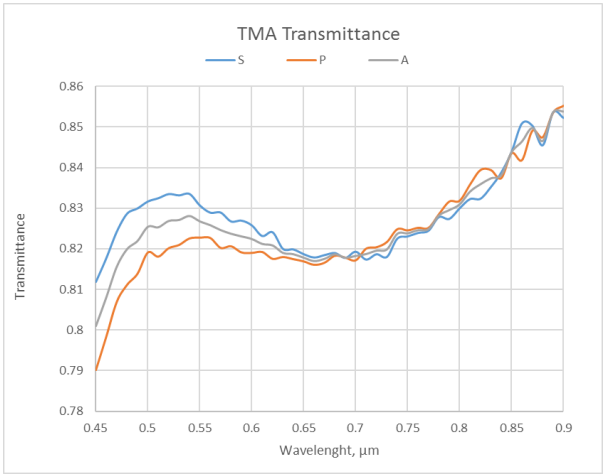

Figure 21 : Transmittance of the complete TMA for central FoV (Protected Silver coating)

CHIEM STATUS AND OUTLOOK

We presented the CHIEM project in which we have developed an engineering model for a hyperspectral instrument to be used on board a satellite mission, operating at 600 km and combining high spatial resolution (GSD 25 m) and hyperspectral (470 – 900 nm, $\Delta\lambda$ < 10 nm) imaging for a swath of 100 Km. The LVF is directly deposited on the large CMOS (4096 x 3072) sensor array, providing several benefits like a higher design flexibility, reduced straylight and better alignment. One third of the array is spent as PAN zone (situated at the bottom and top of the array). Also part of the project is the design of the TMA telescope, which is very compact and allows a wide field of view in both across track and along track direction (> 9.5^o x 7.2^o). Dedicated ROE is developed that is able to read the sensor data at the highest frame rate and resolution and to perform on board data processing.

CHIEM has finalized the manufacturing of the ROE and EGSE and the Hyperspectral sensors, both FSI and BSI, as well as the optical design of the TMA. The project has now passed the Test Readiness Review and has started the extensive characterization of the sensors, which is expected to be finalized in the Summer of 2017.

Operational scenarios are being investigated. Several applications, such as the determination of biophysical parameters, require a high SNR. Due to the narrow spectral bands, the amount of light per pixel is limited. To increase the SNR, the image processing will be optimized and made flexible so that spatial or spectral resolution by binning of pixels can be exchanged for higher SNR. Techniques like PAN-sharpening will be

used to improve the spatial resolution of the LVF images.

Acknowledgement and disclaimer

The CHIEM project acknowledges the support of the Belgian Science Policy Office. It is also a pleasure to thank Luca Maresi from ESA for his inspiring role in the development of LVF instrumentation for remote sensing and his support for the CHIEM project.

The view expressed in this paper can in no way be taken to reflect the official opinion of the European Space Agency.

REFERENCES

1. M. Marshall, P. Thenkabail, Advantage of hyperspectral EO-1 Hyperion over multispectral IKONOS, GeoEye-1, WorldView-2, Landsat ETM+, and MODIS vegetation indices in crop biomass estimation, ISPRS Journal of Photogrammetry and Remote Sensing, Vol. 108, Pages 205–218, Oct. 2015.
2. L. Guanter et al, The EnMAP Spaceborne Imaging Spectroscopy Mission for Earth Observation, Remote Sensing, 7(7), 8830-8857, 2015
3. M. Meini, E. Fossati, L. Giunti, M. Molina, R. Formaro, F. Longo, G. Varacalli, *The PRISMA Mission Hyperspectral Payload*, Proc. 66th Int. Astronautical Congress (IAC 2015), Jerusalem, Israel, Oct.12-16, 2015.
4. C. M. Lee, M. L. Cable, S. J. Hook, R. O. Green, S. L. Ustin, D. J. Mandl, E. M. Middleton, *An introduction to the NASA Hyperspectral InfraRed Imager (HyspIRI) mission and preparatory activities*, Remote Sensing of Environment, Volume 167, Pages 6-19, 2015
5. W. Dierckx, S. Sterckx, I. Benhadj, S. Livens, G. Duhoux, T. Van Achteren, M. Francois, K. Mellabb and G. Saint, *PROBA-V mission for global vegetation monitoring: standard products and image quality*, Int. J. of Remote Sensing, Volume 35, Issue 7, 2014
6. L. de Vos, W. Moelans, J. Versluys, V. Moreau, J.F Jamoye, Jan Vermeiren, L. Maresi, M. Taccola, "The Vegetation Instrument for the PROBA-V Mission" In: Sandau R., Roeser HP., Valenzuela A. (eds) Small Satellite Missions for Earth Observation. Springer, Berlin (2010), Heidelberg
7. L. Maresi, M. Taccola, M. Kohling and S. Livens, *PhytoMapper - Compact Hyperspectral Wide Field of View Instrument*, Proc Small Satellite Missions for Earth Observation, Berlin, Germany, 2010.
8. V. Moreau, C. DeClerq, G. Lousberg, L. Maresi, B. Delauré, *Development of a Compact Hyperspectral/Panchromatic Imager for Management of Natural Resources*, in the 4S symposium, 4-8 June 2012.
9. A. Näsilä et al, *Aalto-1-A Hyperspectral Earth Observing Nanosatellite*, Proc. SPIE 8176, Sensors, Systems, and Next-Generation Satellites XV, 3 October 2011.
10. Conticello et al, *Hyperspectral Imaging for Real Time Land and Vegetation Inspection*, Proc. 4S conference 2016, Malta.
11. A. Lambrechts, P. Gonzalez, B. Geelen, P. Soussan, K. Tack and M. Jayapala, *A CMOS-compatible, integrated approach to hyper- and multispectral imaging*, Proc IEEE Int. Electron Devices Meeting, San Francisco, CA, 15-17 Dec. 2014
12. A. Sima; S. Livens; W. Dierckx, B. Delauré, K. Tack, B. Geelen and A. Lambrechts, *Spatially variable filters — Expanding the spectral dimension of compact cameras for remotely piloted aircraft systems*, Proc IEEE Geoscience and Remote Sensing Symposium, 2014
13. Sima, A., Baeck, P., Nuyts, D., Delalieux, S., Livens, S., Blommaert, J., Delauré, B., Boonen, M., *Compact Hyperspectral Imaging System (COSI) For Small Remotely Piloted Aircraft Systems (RPAS) – System Overview and First Performance Evaluation Results* in Int. Arch. Photogramm. Remote Sens. Spatial Inf. Sci., XLI-B1, 1157-1164, doi:10.5194/isprs-archives-XLI-B1-1157-2016, 2016
14. P. Baeck, J. Blommaert, S. Delalieux, B. Delauré, S. Livens, D. Nuyts, A. Sima, G. Jacquemin and J.P. Goffart, *High reolution vegetation mapping with a novel compact hyperspectral camera system.* In "13th International Conference on Precision Agriculture, St Louis, 2016
15. Livens S., Delauré B., Lambrechts A., Tack N., *Hyperspectral Imager Development using Direct Deposition of Interference Filters*, 4S symposium, 2014
16. X. Wang, et al, *A 2.2M CMOS Image Sensor for High Speed Machine Vision Applications*, proc. SPIE vol.7536, San Jose, Jan. 2010

17. Sedky, S., Witvrouw, A. , Bender H. and Baert, K., "*Experimental determination of the maximum annealing temperature for standard CMOS wafers*", IEEE Trans. Electron Devices 48 (2), 377-385 (2001).

18. Takeuchi, H., Wung , A., Sun, X., Howe, R. T. and King, T.-J. , "Thermal budget limits of quarter-micrometer foundry CMOS for post-processing MEMS devices", IEEE Trans. Electron Devices, 52 (9), 2081-2086 (2005).

19. Macleod, H.A., [Thin-Film Optical Filters, 4th Ed.], Taylor & Francis, 45-52 (2001).